Nanoscale Res Lett (2009) 4:122–129
DOI 10.1007/s11671-008-9211-8

NANO EXPRESS

Ultrafast Carrier Relaxation in InN Nanowires Grown by Reactive Vapor Transport

Andreas Othonos · Matthew Zervos · Maria Pervolaraki

Received: 18 October 2008 / Accepted: 11 November 2008 / Published online: 26 November 2008

Abstract We have studied femtosecond carrier dynamics in InN nanowires grown by reactive vapor transport. Transient differential absorption measurements have been employed to investigate the relaxation dynamics of photogenerated carriers near and above the optical absorption edge of InN NWs where an interplay of state filling, photoinduced absorption, and band-gap renormalization have been observed. The interface between states filled by free carriers intrinsic to the InN NWs and empty states has been determined to be at 1.35 eV using CW optical transmission measurements. Transient absorption measurements determined the absorption edge at higher energy due to the additional injected photogenerated carriers following femtosecond pulse excitation. The non-degenerate white light pump-probe measurements revealed that relaxation of the photogenerated carriers occurs on a single picosecond timescale which appears to be carrier density dependent. This fast relaxation is attributed to the capture of the photogenerated carriers by defect/surface related states. Furthermore, intensity dependent measurements revealed fast energy transfer from the hot photogenerated carriers to the lattice with the onset of increased temperature occurring at approximately 2 ps after pulse excitation.

A. Othonos (✉)
Department of Physics, Research Centre of Ultrafast Science, University of Cyprus, P.O. Box 20537, 1678 Nicosia, Cyprus
e-mail: othonos@ucy.ac.cy

M. Zervos · M. Pervolaraki
Department of Mechanical Engineering, Materials Science Group, University of Cyprus, P.O. Box 20537, 1678 Nicosia, Cyprus

Keywords InN Nanowires · Carrier dynamics · Femtosecond differential absorption spectroscopy · Absorption edge · Reactive vapor transport

Introduction

Semiconductor nanowires (NWs) have received increasing attention over the past years because they constitute an important class of fundamental building blocks for the development of nanotechnology. Semiconductor NWs have been grown from not only group IV elements [1, 2] but also III–V [3–6] and II–VI [7] compound semiconductors including variation of composition and doping along their length and radius. Among the III–V's, nitride (N) semiconductors are especially attractive due to the fact that their energy band-gap can be adjusted over a very wide range e.g., between 0.7 eV for InN up to 6.0 eV in AlN by changing the composition of the ternary semiconductor $In_xAl_{1-x}N$ over $0 \leq x \leq 1$. Semiconductor quantum dots such as InN which have been grown by molecular beam epitaxy (MBE) on GaN have been investigated by Lozano et al. [8] while ultrafast carrier dynamics have also been investigated in self-assembled quantum dots by Rainò et al. [9]. In addition, InN NWs have been grown by a variety of methods [10–14], including reactive vapor transport [10, 11], chemical vapour deposition [12], and molecular beam epitaxy [13]. Similarly, AlN NWs have been obtained using similar methods but the growth of $In_xAl_{1-x}N$ with intermediate band-gaps remains yet to be investigated. Evidently, understanding the growth mechanisms and basic electronic and optical properties of the binary InN and AlN semiconductor NWs is a prerequisite for further investigations of $In_xAl_{1-x}N$ with $0 \leq x \leq 1$. To date the electronic properties of InN NWs such as resistance and

conductivity [15–18] have also been measured, and the InN NWs are found to be n-type with very large carrier densities in the range 10^{18}–10^{22} cm^{-3} and maximum electron mobilities of 300 cm^2/Vs which are lower than those measured in epitaxial InN layers. In addition the optical properties of InN NWs such as their steady-state photoluminescence (PL) spectra have also been measured [14, 19–23] but no detailed, time-resolved-transient spectroscopy measurements have been carried out as in the case of other semiconductor NWs such as InP [24], CdS [25] and GaN [13]. Consequently, in an attempt to systematically investigate N-NWs such as InN, AlN, and $In_xAl_{1-x}N$ with $0 \leq x \leq 1$, we focus on the growth of InN NWs by reactive vapour transport and investigate the nature of the electronic states by time-resolved differential absorption spectroscopy which is a versatile, non-destructive method that can reveal the dominant recombination mechanisms and carrier dynamics [26].

Experimental Procedure

The InN NWs were grown using a chemical vapor deposition (CVD) system that consists of four mass flow controllers (MFC's) and a horizontal tube furnace, capable of reaching a maximum temperature of 1,100 °C. More specifically InN NWs were grown on n^+ Si(111), covered with a thin layer of Au that had a thickness of 1–2 nm. The Au/Si(111) samples had an area ≈ 1 cm^2 and initially the silicon was cleaned in HF, rinsed in de-ionized water and dried prior to the deposition of the Au layer in order to remove the native oxide and surface contamination. The Au layer was deposited via sputtering at a rate of 10 Å/s using an Ar plasma under a pressure $<10^{-4}$ mBar.

In order to grow InN NWs, we used ≈ 0.2 g of fine In powder (Aldrich, Mesh-100, 99.99%) that was loaded in the center of a quartz boat. Two samples of Au/Si(111) were then loaded into the quartz boat; one ≈ 5 mm above the In powder and another ≈ 10 mm downstream from the In powder. Subsequently, the quartz boat was loaded into a quartz tube with a 25-mm diameter, right at its centre and directly above the thermocouple used to measure the heater temperature. After loading the quartz boat at room temperature (RT), nitrogen N_2 (99.999%) was introduced at 500 standard cubic centimetres per minute (sccms) for 5 min in order to purge the tube and eliminate oxygen and moisture. Following this, the temperature was ramped to the desired growth temperature (T_G) over a 30-min interval in a continuous flow of NH_3 at 250 sccms. Upon reaching T_G the flow of NH_3 was maintained at 250 sccms for a further 60 min in order to grow the InN NWs after which the quartz tube was allowed to cool down slowly in a reduced flow of 50 sccms of NH_3 for at least 60 min in order to prevent dissociation of the InN NWs. On reaching RT, the quartz boat was removed from the tube. For the optical measurements, InN NWs were grown directly onto square pieces of quartz with an area of ≈ 1 cm^2. The morphology of the InN NWs was examined with a TESCAN scanning electron microscope (SEM). The crystal structure and the phase purity of the InN NWs were investigated using a SHIMADZU, XRD-6000, X-ray diffractometer and Cu Ka source. A scan of θ–2θ in the range between 10° and 80° was performed for the InN NWs that were grown on Si(111) and quartz.

In this study, the dynamic behavior of carriers in InN nanowires following femtosecond pulse excitation is investigated through the temporal behavior of reflectivity and transmission [27, 28]. The experiments were carried over a wide range of intensities using two different laser amplifier systems. The first amplifier consisted of a self mode-locked Ti:Sapphire oscillator generating 100 fs pulses at 800 nm. A chirped pulsed laser amplifier based on a regenerative cavity configuration is used to amplify the pulses to approximately 1 mJ at a repetition rate of 1 kHz. The second amplifier system consisted also of a mode-locked Ti:Sapphire generating 50 fs pulses at 800 nm. These pulses were amplified with a high repetition rate regenerative amplifier, cavity dumped by an acousto-optic modulator, generating 1 W, 70 fs pulses at 250 kHz center at 800 nm. In both systems the amplified pulses were used to generate 400 nm using nonlinear BBO crystals. A half-wave plate and a polarizer in front of the nonlinear crystals were utilized to control the intensity of the pump incident on the sample. A small part of the fundamental energy was also used to generate a super continuum white light by focusing the beam on a sapphire plate. An ultrathin high reflector at 800 nm was used to reject the residual fundamental pulse from the generated white light to eliminate the possibility of effects by the probe beam. The white light probe beam is used in a non-collinear geometry, in a pump–probe configuration where the pump beam was generated from the frequency doubling of the fundamental. Optical elements such as focusing mirrors were utilized to minimize dispersion effects and thus minimize the broadening of the laser pulse. The reflected and transmission beams are separately directed onto their respective silicon detectors after passing through a band pass filter selecting the probe wavelength from the white light. The differential reflected and transmission signals were measured using lock-in amplifiers with reference to the optical chopper frequency of the pump beam. The temporal variation in the photoinduced absorption is extracted using the transient reflection and transmission measurements, which is a direct measure of the photoexcited carrier dynamics within the probing region [26–28]. Precision measurements of the spot size on the sample of the pump beam along with

measurements of reflection and transmission at the pump wavelength provided accurate estimation of the absorbed fluence ranging from 10 μJ/cm^2 to 5 mJ/cm^2) for the experiments in this study.

Results and Discussion

InN NWs were grown at several temperatures i.e., T_G = 500, 600, 700, 800, 900, and 1,000 °C. The growth of InN NWs on both silicon and quartz resulted into a dark, nearly black layer. Typical SEM images of the InN NWs are shown in Fig. 1a–e. For T_G = 1,000 °C we found that large, spherical droplets of In formed on the surface with diameters ranging from a few micrometers up to many tens of micrometers. There was evidence of wires with large diameters of nearly 1 μm emanating from a few of these large In droplets but these large wires were not abundant. At T_G = 900 °C, we obtained InN wires which are shown in Fig. 1a. The yield was limited and large wires with diameters of ≈1 μm appear to be somewhat twisted. On reducing the temperature to T_G = 800 °C, we observed the growth of spear-like head InN NWs with smaller diameters some of which have a protruding pyramidal head at their ends as can be seen in Fig. 1b. In addition to individual InN NWs, we observed large spherical droplets with diameters up to a few tens of micrometers with InN NWs protruding from their surface as shown in Fig. 1c. Interestingly, the InN NWs grown at T_G = 700 °C do not have protruding pyramidal heads similar to those obtained at T_G = 800 °C

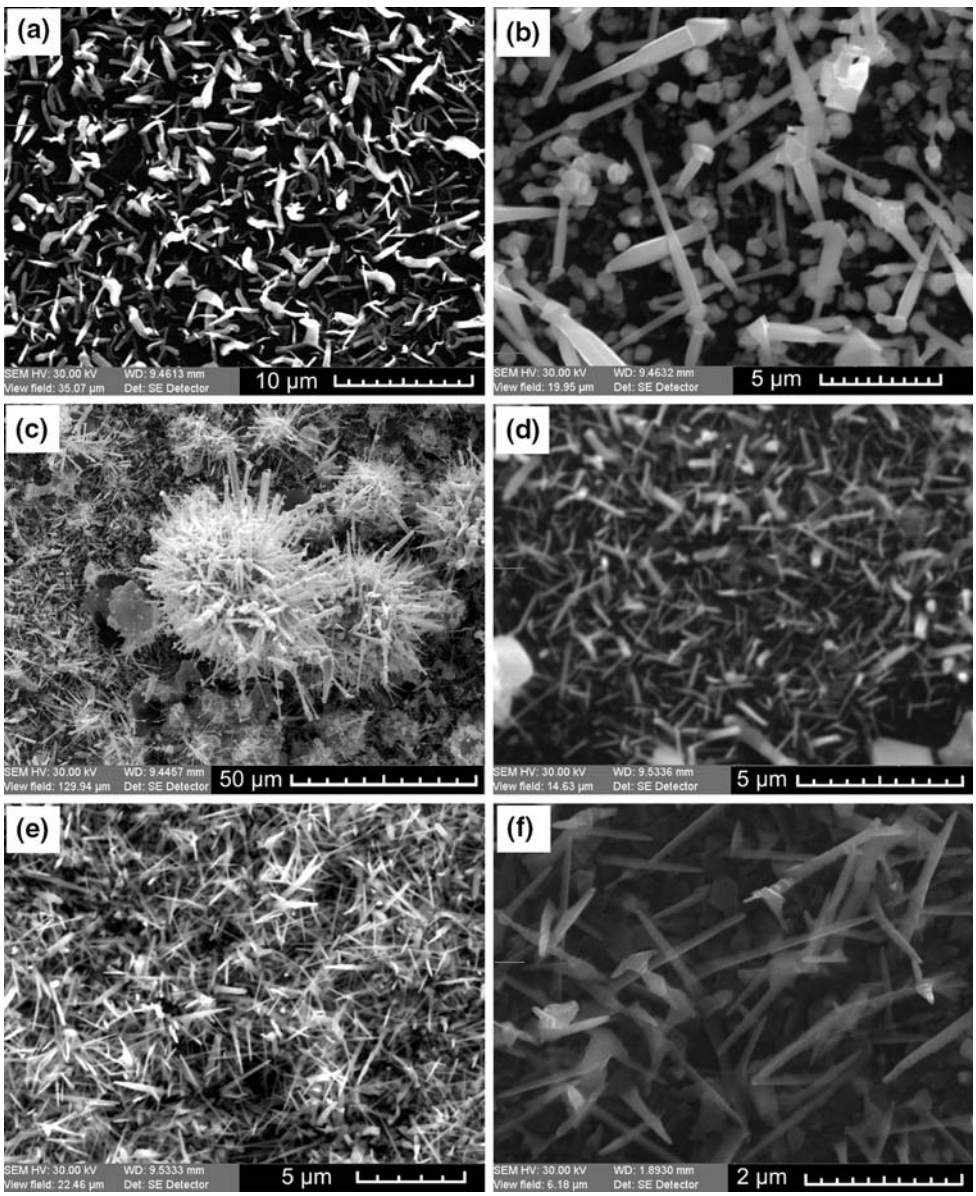

Fig. 1 SEM images of InN NWs grown at (**a**) 900 °C (**b**) 800 °C (**c**) 800 °C (**d**) 700 °C, and (**e**) and (**f**) 600 °C on Au/Si(111)

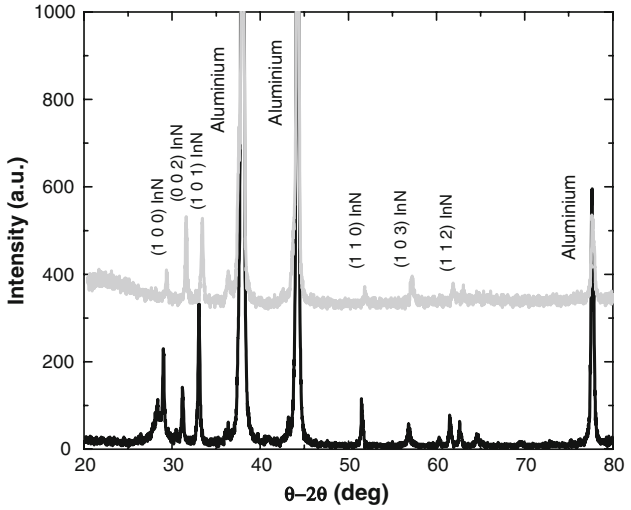

Fig. 2 XRD spectrum of the InN NWs grown at 600 °C on Au/Si(111) lower line and quartz, upper trace

as can be seen in Fig. 1d. We find that the optimum growth temperature for a high yield of straight InN NWs with uniform diameters is $T_G = 600$ °C as shown in Fig. 1e. No NWs were obtained for $T_G = 500$ °C. The spear-like InN NWs grown at $T_G = 600$ °C have lengths of ≈ 5 μm, average diameter of ≈ 100 nm and the coverage is dense. The corresponding XRD pattern of the InN NWs grown on silicon and quartz at $T_G = 600$ °C is shown in Fig. 2.

As stated above, InN NWs have been grown by a variety of methods [10–14]. In particular, InN NWs have been obtained via the reactive vapor transport method using high purity In and NH_3 at various temperatures, i.e., $T = 500$ °C, [20, 11]; $T = 700$ °C, [22, 18]; $T = 750$ °C [10], and $T = 800$ °C [23]. The mechanism of one-dimensional (1D) crystal growth in the case of InN NWs has been explained by Vaddiraju et al. [10] who obtained InN NWs on quartz and polycrystalline AlN at a substrate temperature $T_S = 450$ °C or heater temperature of $T_H = 750$ °C. According to Vaddiraju et al., the 1D crystal growth of the InN NWs occurs by the formation of nucleation sites of InN followed by liquid phase epitaxy through the absorption of In while the radial growth of InN NWs from larger In droplets at higher temperatures of $T_H = 850$ °C ($T_S = 480$ °C) occurs via the formation of multiple nucleation sites of InN on the surface of the droplet giving the characteristic structure shown in Fig. 1c. The trend in the morphology of the InN NWs with temperature shown in Fig. 1a–e is therefore consistent with the findings of Vaddiraju et al. At $T_H = 600$–700 °C, we obtain straight InN NWs while at $T_H = 800$ °C we observe large droplets of In with InN NWs protruding outward in the radial direction from the surface of the droplet. Note that the growth of InN NWs via direct nitridation of In with NH_3 is enhanced using Au on Si(111) which aids the formation of In droplets but it is not indispensable as InN NWs have been also grown directly on quartz and Si(001).

The InN NWs grown at the optimum temperature i.e., $T_G = 600$ °C on silicon and quartz are characterized by the hexagonal wurtzite structure confirmed by the (1 0 0), (0 0 2), (1 0 1), (1 1 0), (1 0 3), and (1 1 2) peaks in both XRD spectra [9, 10] shown in Fig. 2. The side peak at 28.39° corresponds to the (1 1 1) of Si (black line). The double peaks at 77.64° and 77.85° correspond to the Al of the sample holder and possibly to the metallic In, respectively, (black line). The intense reflection peaks correspond to InN NWs whereas the weaker signals correspond to metallic In droplets. From the XRD spectra of Fig. 2 it is evident that no In_2O_3 intensity peaks are present in the NWs grown on both silicon and quartz substrates.

Following the successful growth of InN NWs on silicon and quartz we performed time-resolved differential absorption measurements at room temperature over a wide range of fluences in an attempt to obtain a better understanding of the carrier dynamics in these nanostructures. It is well known that excitation of a semiconductor with above band-gap photons will result in the generation of non-equilibrium carriers with excess kinetic energy corresponding to the difference between excitation photon energy and the band-gap energy. Initially, these photogenerated carriers will be non-thermalized, however carrier–carrier scattering will result in a thermalized distribution within tens of femtoseconds. The carrier temperature of this thermalized distribution will be higher than the lattice temperature. These carriers will then relax to the bottom of the bands via the emission of phonons thus transferring excess energy to the lattice. At the same time, carriers may be captured by various defects, impurities, or surface states that are within the interaction region. Eventually these photogenerated carriers recombine via radiative or non-radiative mechanisms thus bringing the system back to its equilibrium state.

In this study, the excitation of the NWs was accomplished with an ultrafast laser pulse at 400 nm corresponding to 3.1 eV photons which is much higher than the energy band-gap of InN. This excess kinetic energy resulted in generating carriers located high in the energy band structure of the NWs. Figure 3 shows typical differential absorption measurements as a function of time delay between the excitation and the probing pulse under the fixed pump fluence of 50 μJ/cm^2 at various probing photon wavelengths.

Clearly evident from the time-resolved data, there is a complex behavior in the induced absorption which depends on the probing photon wavelength. For probing wavelengths shorter than 750 nm, there is a sharp drop in the induced absorption signal followed by a recovery toward equilibrium. However, with increasing probing wavelength the minimum signal decreases and eventually a positive contribution to the absorption changes becomes dominant.

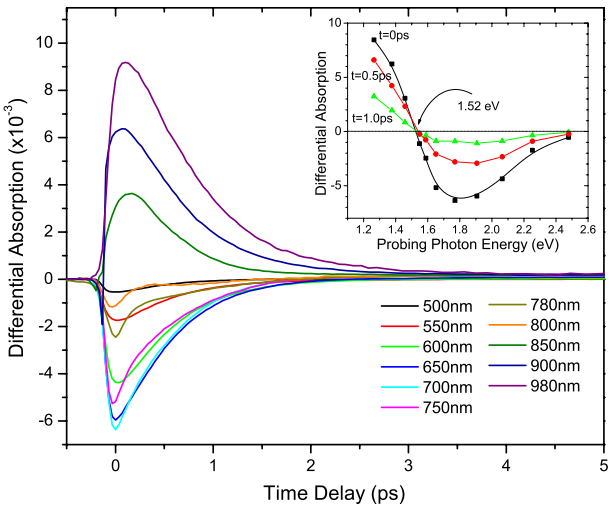

Fig. 3 Differential absorption signal versus time delay for different photon wavelengths in InN NWs. Photoexcitation was accomplished with 3.1 eV photons under a pump fluence of 50 μJ/cm^2 at room temperature. The inset shows the differential absorption signal as a function of probing photon energy at time delays of 0, 0.5, and 1.0 ps

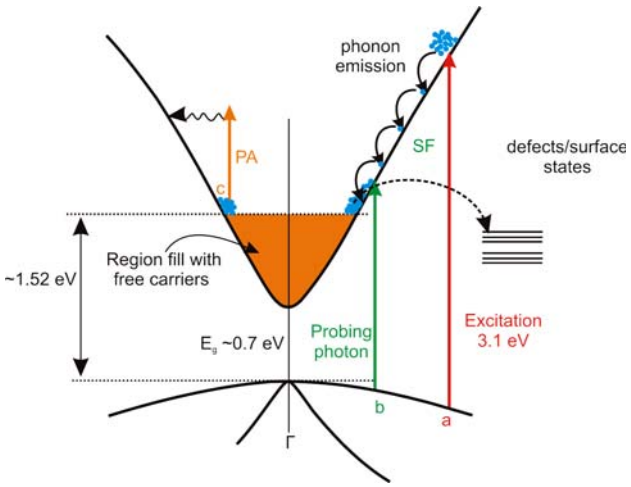

Fig. 4 A schematic diagram of a model explaining femtosecond pulse excitation at 3.1 eV (see vertical arrow "a") and subsequent relaxation of the photexcited carriers in the InN NWs. The vertical arrow "b" indicate the probing photon where coupling between the valence and occupied conduction band is established and thus state filling is observed. The vertical arrow "c" represents secondary excitations (PA) of the carriers by the probe pulse

This observed nontrivial behavior in the time-resolved data is attributed to an interplay between the two effects of state filling (SF) and photoinduced absorption (PA). Following excitation of carriers from the valance to the conduction band, it results in the occupation of normally unoccupied states thus reducing the absorption which appears as a negative absorption change in transient measurements (SF). Therefore photoexcitation of the carriers with an ultrafast pulse provides the means of monitoring the temporal evolution of the occupied states and more specifically the relaxation of the photoexcited carriers out of these states. In addition to the negative SF described above, there are also effects due to secondary excitations of the photogenerated carriers to higher energy states induced by the probing laser pulse. This mechanism will be observed as a positive change in absorption (PA) with its strength depending on the coupling efficiency and the number of carriers present in the initial coupled energy state. In time-resolved absorption measurements, both effects may be present with their relative contributions depending on the energy states of the material under investigation.

For the InN NWs used in this work clearly evident from transient absorption data (Fig. 3), SF is the main contribution for photon wavelengths between 500 and 750 nm, where direct coupling from the valence to the conduction probing state is possible (Fig. 4 see line b). On the other hand, for probing wavelengths >830 nm a positive photoinduced absorption is the dominant effect where direct coupling from the valence to the conduction band is not possible because of the already occupied states in the conduction band from the free carriers intrinsic to the fabrication of the NWs [15–18] and the injected photogenerated carriers by the pump laser pulse. A simple schematic diagram of a model explaining the behavior of the InN NWs following femtosecond pulse excitation is shown in Fig. 4. The diagram shows a representation of the band diagram of InN [29] around the Γ point of the Brillouin zone.

The accepted fundamental band-gap of InN is about 0.7 eV [30]; however, due to a large free electron density present associated with the fabrication of the NWs, it results in the occupation of states near the bottom of the conduction band. As a consequence the interband absorption edge energy is much higher than the actual band-gap energy. This is clearly seen as the zero crossing point (~1.52 eV) in the inset of Fig. 3 and is associated with the transition point between state filling and photoinduced absorption. We should point out that extrapolation of the square of the optical absorption coefficient obtained from optical absorption measurement on the NWs (see Fig. 5) revealed an absorption edge energy of approximately 1.35 eV. The larger value of 1.52 eV determined using transient absorption measurements is due to the additional injected carrier density during photoexcitation of the NWs by the pump femtosecond laser pulse.

The lowest conduction band of InN is highly nonparabolic [30] due to the k–p interaction across the narrow direct gap between the conduction and valence band. A dispersion relation for the conduction band of InN is given in reference [30]

$$E_C(k) = E_g + \frac{\hbar^2 k^2}{2m_0} + \frac{1}{2}\left[\left(E_g^2 + 4E_p\frac{\hbar^2 k^2}{2m_0}\right)^{1/2} - E_g\right]$$

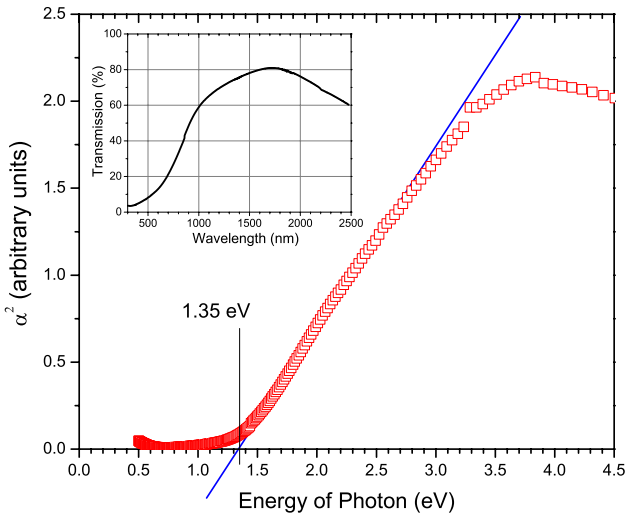

Fig. 5 A variation of the square of the optical absorption coefficient against the photon energy for the InN NWs. The extrapolated absorption edge is approximately 1.35 eV. The inset figure shows the optical transmission data for the InN NWs

where $E_g = 0.7$ eV is the band-gap energy, $E_p \sim 10$ eV is an energy parameter related to the interaction momentum matrix element. Using the above relation, we may estimate the electron carrier density. According to the Fermi exclusion principle, optical transitions can only occur for photon energies higher than the energy needed for electrons to make vertical transitions from the valence band up to the Fermi surface in the conduction band. The increase in Fermi energy with increasing electron concentration is given by the dispersion relation in the above equation evaluated at the Fermi wave vector $k_F = (3\pi^2 N)^{1/3}$, where N is the electron density. Using the value of 1.35 eV for E_C in the above equation we obtain an electron density of 0.91×10^{20} cm^{-3} corresponding to the intrinsic electron density in the InN NWs. On the other hand, the value of 1.52 eV gives a carrier density of 1.48×10^{20} cm^{-3} corresponding to the total number of carriers following the injection of photogenerated carriers by the ultrafast laser pulse at fluence of 50 μJ/cm^2. Therefore, the estimated carrier injected density at this fluence in the NWs was approximately 0.57×10^{20} cm^{-3}. Similar measurements at the lowest fluence (10 μJ/cm^2) used in this study gave an absorption edge at 1.39 eV corresponding to an injected carrier density of $\sim 0.12 \times 10^{20}$ cm^{-3} in agreement with the above results.

To obtain a better understanding of the carrier dynamics in these NWs we have performed intensity measurements over a wide range of fluences from 10 μJ/cm^2 to 5 mJ/cm^2. Typical results of the peak differential absorption as a function of fluence are shown in Fig. 6 for the two extreme probing wavelengths. Figure 6a corresponds to probing with 500 nm where direct coupling from valence to

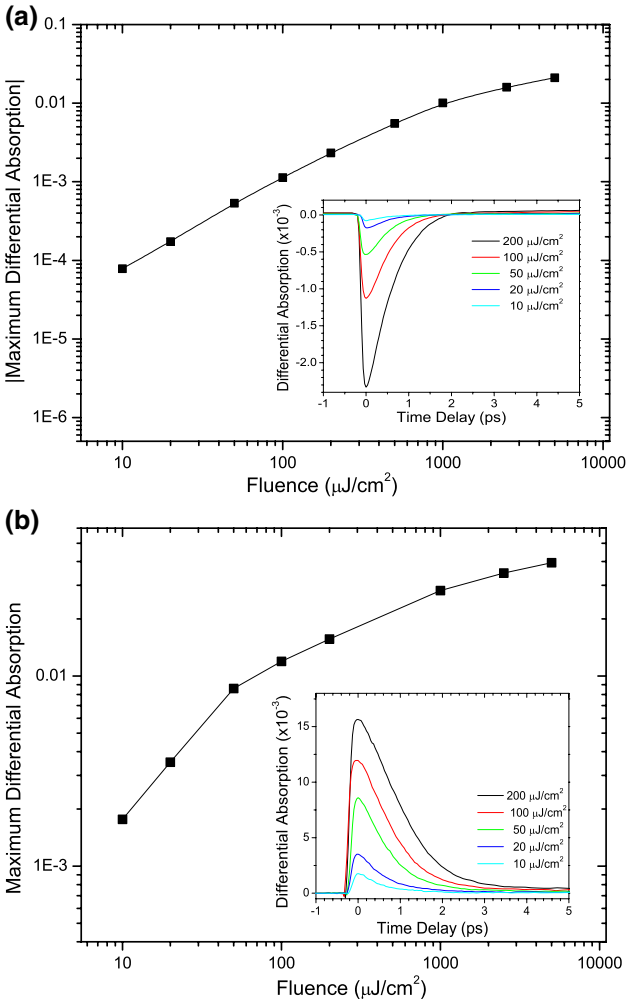

Fig. 6 Plots of the maximum differential absorption signal as a function of the fluence at two probing wavelengths (**a**) 500 nm, and (**b**) 980 nm. The insets in both graphs show the actual differential absorption measurements for various fluence as a function of optical delay between the pump and probe beams

conduction band is allowed, thus state filling is the observed process. The plot reveals a linear dependence on the fluence up to value of 1,000 μJ/cm^2 at which point saturation appears to begin.

Furthermore, the recovery of the negative differential absorption appears to be single exponential over the entire fluence with the decay constant increasing with increasing fluence as seen in Fig. 7. Transient differential absorption intensity measurements at the longer probing wavelengths where we are actually probing the photogenerated carriers following relaxation near the absorption edge also revealed a nonlinear behavior as a function of fluence (Fig. 6b). It appears that the maximum differential absorption begins some type of saturation at the fluence value of 50 μJ/cm^2. The possibility of Auger has been ruled out given that the recovery time constant increases with increasing fluences. One possible explanation is due to absorption saturation

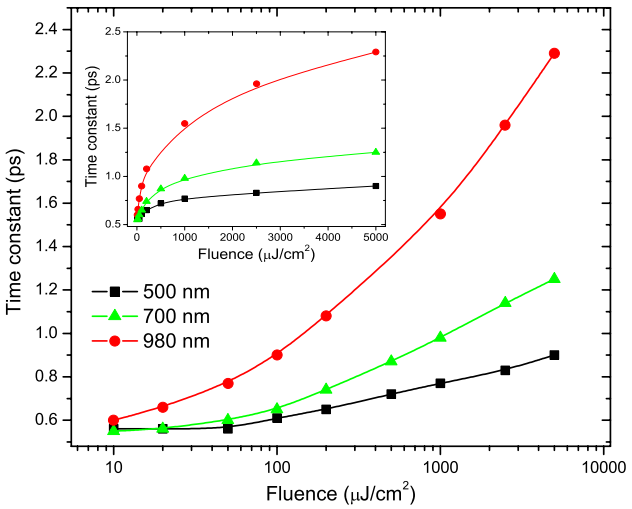

Fig. 7 Plots of time constants obtained from single exponential fits to the recovery of transient differential absorption signal as a function of the fluence for different probing wavelengths. The inset shows the same data plotted as a function of fluence on a linear scale for clarification of the behavior

with increasing incident pump fluence; however, this does not explain the nearly linear behavior seen in Fig. 6a. The most likely reason for the above behavior is that the photogenerated carriers, as they undergo energy relaxation toward the absorption edge, they are captured by defect/surface-related states reducing the carrier density reaching the probing region. This is in agreement with the results of the intensity measurements of Fig. 6a where the behavior is nearly linear for the higher lying energy states (500 nm).

In Fig. 7, we display the time constants obtained from a single exponential fit to the recovery of the transient differential absorption measurements as a function of incident fluence on the NWs. For clarification purposes the inset shows the same data plotted against the fluences on a linear scale. The first key observation from these data is the value of the time constant ($\sim$600 fs) at the lowest fluences. The time constants determined from transient differential absorption measurements for the long probing wavelength 980 nm provide a direct measure of the decay time constant for the photogenerated carriers following their energy relaxation to the optical absorption edge. This appears to be very fast and most likely a non-radiative decay into defect/surface-related states in the NWs. Furthermore, this time constant is increasing in a nonlinear fashion with increasing fluence as seen in Fig. 7. Similarly, the time constants extracted when probing higher energy states are also increasing with increasing fluence.

To further investigate the dynamics near the transition point between state filling and free carrier absorption time-resolved differential absorption measurements at various fluences were taken with probing photon energy near that region. Figure 8a and b show some of these measurements.

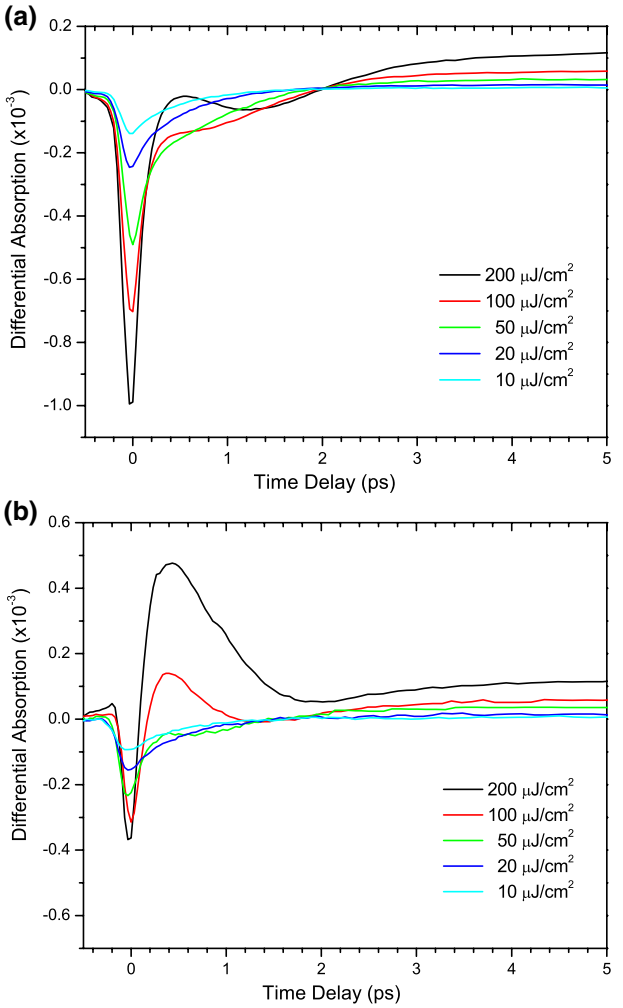

Fig. 8 Differential absorption signal versus time delay for different fluence in InN NWs near the absorption edge. **a** probing photon wavelength at 780 nm **b** probing photon wavelength at 800 nm

Evident from these figures is the nonlinear behavior as a function of fluence. At the lowest fluences the temporal response of the differential absorption suggests state filling is the main contribution.

However, with increasing fluence there appears a positive contribution affecting the normal exponential recovery of state filling. This effect becomes more dramatic with increasing fluence with the positive contribution becoming larger and more pronounced as clearly seen for the 800 nm probing wavelength. This behavior is attributed to the complex relationship between the effects of state filling, band-gap renormalization, and free carrier absorption. We should point out that for the highest fluence, there appears to be a positive contribution to the differential absorption which remains constant and persists for times longer than 500 ps which corresponds to the maximum travel of the translation state in the pump–probe setup. This contribution is most likely due to an increase in the lattice temperature

of the InN NWs. The onset of the lattice temperature contribution appears to occur around 2 ps which suggests that the excess energy from the photoexcited hot carriers has transferred to the lattice within this time scale.

In conclusion, we have investigated ultrafast carrier dynamics in InN NWs grown via chemical vapor deposition. CW optical transmission data revealed the interface between intrinsic free carriers and the free states in the conduction band occurs at 1.35 eV corresponding to an intrinsic electron density of 0.91×10^{20} cm^{-3}. Femtosecond differential absorption spectroscopy determined the interface between the total number of carriers present and the free states for fluence of 50 $\mu J/cm^2$ at 1.52 eV, corresponding to an injected carrier density of 0.57×10^{20} cm^{-3}. Furthermore, intensity measurements revealed that the photogenerated carriers following their energy relaxation near the absorption edge relax into defect/surface-related states on a picosecond time scale. The exact value depends on the number of photogenerated carriers injected into the NWs. Interesting nonlinear behavior of the temporal differential absorption due to an interplay between state filling, band-gap renormalization, and free carrier absorption have been observed near the optical absorption edge of the InN NWs. Finally, the onset of positive increase in differential absorption which persists for a long period of time suggests that the generated carriers transfer their energy to the lattice within approximately 2 ps.

Acknowledgments The study in this article was partially supported by the research programs; EPYNE/0504/06, ERYAN/0506/04, and ERYNE/0506/02 funded by the Cyprus Research Promotion Foundation in Cyprus. The authors wish to thank Prof. John Giapintzakis, Head of the Mechanical Engineering Department, for using his laboratory, sputtering unit, and materials.

References

1. Y. Cui, C.M. Lieber, Science **291**, 851 (2001). doi:10.1126/science.291.5505.851
2. Y. Wu, R. Fan, P. Yang, Nano. Lett. **2**, 83 (2002). doi:10.1021/nl0156888
3. K. Hiruma, M. Yazawa, T. Kakibayashi, J. Appl. Phys. **77**, 447 (1995). doi:10.1063/1.359026
4. X. Duan, Y. Huang, Y. Cui, J. Wang, C.M. Lieber, Nature **409**, 66 (2001). doi:10.1038/35051047
5. M.T. Björk, B.J. Ohlsson, T. Sass et al., Appl. Phys. Lett. **80**, 1058 (2002). doi:10.1063/1.1447312
6. Y. Huang, X. Duan, Y. Cui, C.M. Lieber, Nano. Lett. **2**, 101 (2002). doi:10.1021/nl015667d
7. R. Solanki, J. Huo, J.L. Freeouf, B. Miner, Appl. Phys. Lett. **81**, 3864 (2002). doi:10.1063/1.1521570
8. J.G. Lozano, A.M. Sánchez, R. García, S. Ruffenach, O. Briot, D. González, Nanoscale Res. Lett. **2**, 442 (2007). doi:10.1007/s11671-007-9080-6
9. G. Rainò, G. Visimberga, A. Salhi, M.T. Todaro, M.D. Vittorio, A. Passaseo, R. Cingolani, M. De Giorgi, Nanoscale Res. Lett. **2**, 509 (2007). doi:10.1007/s11671-007-9092-2
10. S. Vaddiraju, A. Mohite, A. Chin, M. Meyyappan et al., Nano. Lett. **5**, 1625 (2005). doi:10.1021/nl0505804
11. M. He, S.N. Mohammad, J. Vac. Sci. Technol. B **25**, 940 (2007). doi:10.1116/1.2740275
12. H. Parala, A. Devi, F. Hipler, E. Maile, A. Birkner, H.W. Becker, R.A. Fischer, J. Cryst. Growth **231**, 68 (2001). doi:10.1016/S0022-0248(01)01463-4
13. J.B. Schlager, K.A. Bertness, P.T. Blanchard, L.H. Robins, A. Roshko, N. Sanford, J. Appl. Phys. **103**, 124309 (2008). doi:10.1063/1.2940732
14. L.W. Yin, Y. Bando, D. Golberg, M.S. Li, Adv. Mater. **16**, 1833 (2004). doi:10.1002/adma.200306684
15. C.-Y. Chang, G.-C. Chi, W.-M. Wang, L.-C. Chen, K.-H. Chen, F. Ren, S.J. Pearton, Appl. Phys. Lett. **87**, 093112 (2005). doi:10.1063/1.2037850
16. C. Blömers, T. Schäpers, T. Richter, R. Calarco, H. Lüth, M. Marso, Phys. Rev. B **77**, 201301R (2008). doi:10.1103/PhysRevB.77.201301
17. H. Ahn, Y.P. Ku, Y.C. Wang, C.H. Chuang, S. Gwo, Appl. Phys. Lett. **91**, 163105 (2007). doi:10.1063/1.2800292
18. G. Cheng, E. Stern, D. Turner-Evans, M.A. Reed, Appl. Phys. Lett. **87**, 253103 (2005). doi:10.1063/1.2141927
19. J. Zhang, B. Xu, F. Jiang, Y. Yang, J. Li, Phys. Lett. A **337**, 121 (2005). doi:10.1016/j.physleta.2005.01.048
20. Z.H. Lan, W.M. Wang, C.L. Sun, S.C. Shi, C.W. Hsu, T.T. Chen, K.H. Chen, C.C. Chen, Y.F. Chen, L.C. Chen, J. Cryst. Growth **269**, 87 (2004). doi:10.1016/j.jcrysgro.2004.05.037
21. C.H. Lang, L.C. Chen, J.S. Hwang, K.H. Chen, Y.T. Hung, Y.F. Chen, Appl. Phys. Lett. **81**, 22 (2002). doi:10.1063/1.1490636
22. M.C. Johnson, C.J. Lee, E.D. Bourret-Courchesne, Appl. Phys. Lett. **85**, 5670 (2004). doi:10.1063/1.1831563
23. H.Y. Xu, Z. Liu, X.T. Zhang, S.K. Hark, Appl. Phys. Lett. **90**, 113105 (2007). doi:10.1063/1.2712801
24. S. Crankshaw, S. Reitzenstein, L.C. Chuang, M. Moewe, S. Münch, C. Böckler, A. Forchel, C. Chang-Hasnain, Phys. Rev. B **77**, 235409 (2008). doi:10.1103/PhysRevB.77.235409
25. L.V. Titova, T.B. Hoang, H.E. Jackson, L.M. Smith, J.M. Yarrison-Rice, J.L. Lensch, L.J. Lauhon, Appl. Phys. Lett. **89**, 053119 (2006). doi:10.1063/1.2266414
27. A. Othonos, J. Appl. Phys. **83**, 1789 (1998). doi:10.1063/1.367411
28. A. Othonos, E. Lioudakis, U. Philipose, H.E. Ruda, Appl. Phys. Lett. **91**, 241113 (2007). doi:10.1063/1.2825290
29. A. Othonos, E. Lioudakis, A.G. Nassiopoulou, Nanoscale Res. Lett. **3**, 315 (2008). doi:10.1007/s11671-008-9159-8
30. I. Mahboob, T.D. Veal, L.F.J. Piper, C.F. McConville, H. Lu, W.J. Schaff, J. Furthmüller, F. Bechstedt, Phys. Rev. B **69**, 201307 (2004). doi:10.1103/PhysRevB.69.201307
31. J. Wu, W. Walukiewicz, K.M. Yu, J.W. Ager III, E.E. Haller, H. Lu, W.J. Schaff, Y. Saito, Y. Nanishi, Appl. Phys. Lett. **80**, 3967 (2002). doi:10.1063/1.1482786